Near-Infrared Light-Emitting Diodes utilizing a Europium-Activated Calcium Oxide Phosphor with External Quantum Efficiency of up to 54.7%

Jianwei Qiao, Shuai Zhang, Xinquan Zhou, Weibin Chen, Romain Gautier, Zhiguo Xia

Near-infrared light-emitting diode utilizing europium-activated calcium oxide phosphor with external quantum efficiency of up to 54.7%

Jianwei Qiao, Shuai Zhang, Xinquan Zhou, Weibin Chen, Romain Gautier, and Zhiguo Xia*

J. W. Qiao, S. Zhang, X. Q. Zhou, W. B. Chen, Prof. Z. G. Xia
State Key Laboratory of Luminescent Materials and Devices and Institute of Optical Communication Materials, Guangdong Provincial Key Laboratory of Fiber Laser Materials and Applied Techniques, School of Materials Science and Engineering, South China University of Technology, Guangzhou, 510641, China.
E-mail: xiazg@scut.edu.cn

Prof. R. Gautier
Université de Nantes, CNRS, Institut des Matériaux Jean Rouxel, IMN, F-44000 Nantes, France.

Prof. Z. G. Xia
School of Physics and Optoelectronics, South China University of Technology, Guangzhou, Guangdong, 510641, China.

Keywords: near-infrared luminescence, phosphor, light-emitting diodes

Abstract:

Near-infrared (NIR) luminescence materials with broadband emissions are necessary for the development of light-emitting diodes (LEDs) based light sources. However, most known NIR emitting materials are limited by their low external quantum efficiency. Here, we report how the photoluminescence quantum efficiency of europium-activated calcium oxide (CaO:Eu) NIR phosphor can be significantly improved and stabilized at operating temperatures of LEDs. A carbon paper wrapping technology was innovatively developed and used during the solid-state sintering to promote the reduction of Eu^{3+} into Eu^{2+}. In parallel, the oxygen vacancies in the CaO lattice were repaired utilizing GeO_2 decomposition. Through this process, a record high external quantum efficiency of 54.7% at 740 nm is obtained with a thermal stability greatly improved from 57% to 90% at 125 °C. The as-fabricated NIR-LEDs reach a photoelectric efficiency of 100 mA@23.4% and an output power of 100 mA@319.5 mW, which are also the record values reported so far. This discovery of high-performance phosphors will open new research avenues for broadband NIR LEDs light sources in a variety of photonics applications.

1. Introduction

Near-infrared (NIR) light sources play important roles in various crucial fields, such as biomedical imaging, remote sensing, night vision and food monitoring, etc..[1] While organic fluorophores, quantum dots, polymers and metal halides have shown benefits as NIR emitters, they so far failed to produce efficient NIR light sources because of their stability issues, low photoluminescence quantum yield (QY) and/or narrowband emissions.[2] In the light of high stability and low fabrication cost, high QY and tunable emission, inorganic luminescent materials show a great potential in the fabrication of highly efficient NIR phosphor-converted light-emitting diodes (LEDs) with broadband emissions.[3]

Recently, Cr^{3+} activated inorganic solid-state phosphors have attracted much attentions due to the broadband NIR emission.[3-4] However, the low absorption strengths of the parity forbidden *d-d* transitions of Cr^{3+} activators lead to low external quantum efficiency (EQE). For example, $Ca_3Sc_2Si_3O_{12}:Cr^{3+}$ and $Na_3ScF_6:Cr^{3+}$ possess a very high internal quantum efficiency (IQE) of 92.3% and 91.5% respectively, but low EQE values of 25.5% and 40.8% fail to meet the requirement of practical applications.[5] Higher EQE values have been also obtained in some NIR phosphors, such as $LaMgGa_{11}O_{19}:Cr^{3+}$ (42.5%) and $SrGa_{12}O_{19}:Cr^{3+}$ (45%), but EQE still remain lower than 50%.[6] In contrary, Eu^{2+} activated solid-state phosphors with the parity-allowed *d-f* emission are normally endowed with strong absorption and high EQE, and have been commercialized for solid-state lighting.[7] Unfortunately, seldom Eu^{2+}-doped NIR emitters have been discovered, and the existed emitters exhibit much lower emission efficiency (EQE < 15%) and weaker thermal stabilities.[1d, 8] Therefore, developing high efficiency and high thermal stability NIR phosphors has become a crucial challenge for the ongoing developments of broadband NIR-LED light sources.

To reach such requirements of high efficiency and high stability for NIR Eu-doped phosphors, two important parameters must be considered: (i) the formation of luminescence "killer" Eu^{3+} should be prevented,[9] and (ii) the structural rigidity as well as the construction of defects should be controlled.[10] Europium-activated calcium oxide phosphor exhibiting a rigid structure, a binary oxide composition and a NIR emission appeared to be of interest. However, the coexistence of the Eu^{2+} and Eu^{3+} centers in this material is known to be responsible of its low quantum efficiency.[11] Here, we succeed to improve simultaneously the efficiency and thermal stability of CaO:Eu NIR phosphor to reach the commercial application standards. By introducing carbon paper or using a graphite crucible to further optimize the reduction process under N_2+H_2 gas, more Eu^{3+} luminescent killers can be reduced into beneficial Eu^{2+} emission centers. Furthermore, GeO_2 addition during the synthesis effectively eliminates the oxygen vacancies in CaO:Eu due to the insertion of O^{2-} ions from the GeO_2

decomposition. These conditions finally lead to an unprecedent improvement of the EQE by three times from 17.9% to 54.7%, and a giant enhancement of the thermal stability of about 33% for the treated material at 125 °C compared with the untreated materials. We further proved that the defect elimination mechanism also accounted for the improvement of the thermal stability. Such results suggest the general possibility to design new doped phosphors for emerging high-power applications.[7a, 10c] The design strategies proposed here can be extended to develop other europium-activated inorganic phosphors for efficient and high-power LED light source applications.

2. Results and discussion

As shown in **Figure 1**a, the as-prepared CaO:Eu phosphor via the optimized technique exhibits a broad emission band centered at 740 nm under 470 nm excitation, attributed to the characteristic $4f^6 5d^1 \rightarrow 4f^7$ transition of Eu^{2+}. The corresponding photoluminescence excitation (PLE) spectrum monitored at 740 nm contains two bands peaking at 245 and 470 nm, which are ascribed to the $4f^7(^8S_{7/2}) \rightarrow 4f^6 5d(T_{2g})$ and $4f^7(^8S_{7/2}) \rightarrow 4f^6 5d(E_g)$ transitions respectively.[11] The PL intensity of sample wrapped with carbon paper or placed in graphite crucible (marked as CaO:Eu@C) shows a significant enhancement compared with the PL intensity of the initial CaO:Eu phosphor. Furthermore, the integrated PL intensity of GeO_2 treated sample (marked as CaO:Eu@C+GeO_2) is more than 2.7 times higher than that of the untreated sample. In addition, the bulk color of CaO:Eu turns from light purple to dark purple under natural light illumination. These results suggest that enhancing the reduction via carbon paper wrapping technology and adding GeO_2 can be acted as an effective approach to increase the luminescence intensities of CaO:Eu. As shown in the Figure S1a (Supporting Information), the structure remains invariable, as all the diffraction peaks are well consistent with the calculated patterns of CaO. Rietveld methods used on powder XRD data also demonstrate that the GeO_2 addition does not modify the phase, even at a high concentration of 8% (Figure S1b).

Figure 1b shows the IQE, EQE and absorption efficiency (Abs) of CaO:Eu and CaO:Eu@C+$x$$GeO_2$ (x = 0-6%) phosphor, respectively. As one can see, all the samples possess a relatively high absorption efficiency at around 70%, which coincides with the values measured from the diffuse reflectance spectra (Figure S2a) and helps to obtain high EQE values. Obviously, the IQE and EQE values increase for the samples treated by carbon and GeO_2, and reach a maximum at x = 4%. The EQE value (54.7%) of CaO:Eu@C+4%GeO_2 is about 3-fold higher than that of CaO:Eu (17.9%) counterpart. In particular, CaO:Eu@C+4%GeO_2 exhibits distinct advantages in both Abs and EQE values compared with the currently reported most efficient NIR phosphors, such as $Ca_3Sc_2Si_3O_{12}:Cr^{3+}$, $Na_3ScF_6:Cr^{3+}$ and $LaMgGa_{11}O_{19}:Cr^{3+}$, as shown in **Figure 1**c and Table S1 (Supporting Information).[5-6]

For the purpose of getting deep insights into the EQE enhancement mechanism, the valence state of Eu was analyzed in detail. From the Eu-*L3* edge X-ray absorption near-edge structure (XANES) spectra in Figure S3a, all the samples contain two peaks centered at 6974 and 6983 eV, ascribing to the $2p_{3/2} \rightarrow 5d$ transition of Eu^{2+} and Eu^{3+}, respectively.[9] The relative intensity of Eu^{2+} absorption band increased obviously after carbon treatment and is further enhanced with GeO_2 addition. Accordingly, the high resolution XPS spectra are recorded in the energy region of the Eu-3*d* transition and presented in Figure S3b. This range consists of four peaks, which are derived from the 3*d* state spin-orbit splitting of both Eu^{3+} and Eu^{2+} ions into $3d_{5/2}$ and $3d_{3/2}$. The peak at the binding energy of 1134, 1164 eV and 1124, 1154 eV correspond to the Eu^{3+} and Eu^{2+} ions, respectively. Similar change trend is observed for the XPS intensity of Eu^{2+} and Eu^{3+}, which once again confirms the effective reduction of Eu^{3+} to Eu^{2+}. Based on above analyses, the increase of Eu^{2+}/Eu^{3+} ratio in the CaO:Eu@C+4%GeO_2 phosphor is the major reason for the improved EQE, and such a schematic model is partially demonstrated in **Figure 1**d.

Since the decay time is directly proportional to the luminescence efficiency, the decay curves monitored at 740 nm are measured and presented in Figure S4 under pulse laser excitation at 450 nm.[12] All the decay curves can be well-fitted by the bi-exponential functions:[13]

$$I = A_1 \exp\left(-\frac{t}{\tau_1}\right) + A_2 \exp\left(-\frac{t}{\tau_2}\right) \quad (1)$$

where A_1, A_2 is the corresponding fitting constant; I is luminescence intensity; τ_1 and τ_2 are lifetimes for the fast and slow components; t is time. The details of fitting results are listed in Table S2. The decay time reveals an increasing tendency for CaO:Eu (0.8 μs), CaO:Eu@C (0.99 μs) and CaO:Eu@C+4%GeO_2 (1.47 μs) phosphors, in agreement with the trend of emission intensity in Figure 1a. It is worth noting that only one type of Eu^{2+} luminescent centers existed in CaO:Eu lattice, while the decay curves were well fitted by bi-exponential functions. This mismatch between the numbers of luminescent centers and fitting index is due to the additional nonradiative transitions originated from lattice thermal vibration participating in the luminescence process. Especially, the sharp increase in lifetime for CaO:Eu@C+4%GeO_2 sample is attributed to the restraint of nonradiative transition process, which will be discussed in detail in the thermal quenching section.[12]

Another key assessment index for an excellent phosphor is the thermal quenching (TQ) behavior. **Figure 2**a shows the temperature dependent integrated emission intensity for the CaO:Eu, CaO:Eu@C and CaO:Eu@C+4%GeO_2 phosphors measured at temperatures ranging from 25 to 125 °C. The PL intensity of all the samples decreases with increasing temperature due to the TQ effect. It should be noted that both CaO:Eu and CaO:Eu@C exhibit a similar poor thermal stability. This result indicates that strengthening the reducing atmosphere with carbon paper or graphite crucible alone can hardly improve the thermal stability of CaO:Eu. By contrast, the thermal stability of CaO:Eu@C+$x$$GeO_2$ (x = 1%-6%) samples are greatly improved, as shown in **Figure 2**b and Figure S5. In particular, the integrated intensity of

CaO:Eu@C+4%GeO_2 remains 90% at 125 °C of the initial intensity at room temperature. Such superior thermal stability is conducive to its application in high-power NIR light source.

According to the thermal ionization model proposed by Dorenbos, the thermal stability is decided, in great extent, by the energy barrier ΔE between the conduction band and 5*d* level of Eu^{2+}.[14] Hence, the variation of bandgap is of first importance. **Figure 2**c shows the plots of $(\alpha h\nu)^2$ versus photo energy $h\nu$ based on the diffuse reflectance spectra of the materials (Figure S2b). The bandgaps of all the samples determined by the transformed Kubelka-Munk function remain almost unchanged with the value of about 3.86 eV.[15] This result is expected because it can be inferred from the fact that Ge^{4+} ions do not enter the CaO lattice. In addition, the same emission peaks at 740 nm (Figure 1a) indicates that the 5*d* energy level of each sample does not change. Therefore, another quenching mechanism must be considered. Recent studies revealed that energy transfer from the thermally activated defect levels to the Eu^{2+} 5*d*-band can enhance thermal stability.[7a, 10c] This model involves two basic factors: defect level and thermoluminescence. As such, DFT calculations were performed to determine the defect types in CaO:Eu phosphor, as illustrated in **Figure 2**d and Table S3. Such calculations show that oxygen vacancies are easily formed due to a negative formation energy (-3.27 eV) of V_O, while the defect V_{Ca} can be hardly generated with a formation energy of 5.69 eV. Moreover, the strong electron paramagnetic resonance (EPR) signals observed around g = 1.996 further approve the existence of V_O (**Figure 2**e).[8b, 16] Nevertheless, no spectral signal was detected from both the 2- and 3-dimensional thermoluminescence (TL) measurement for the selected samples, as shown in Figure S6. These results suggest that the defect levels do not assist the thermal stability for the CaO:Eu phosphor.

As exhibited in Figure 2e, the intensity of EPR signal for CaO:Eu@C+4%GeO_2, which shows the best thermal stability, is significantly weaker than the ones of CaO:Eu and CaO:Eu@C (**Figure 2**a). Compared with the EPR spectra of CaO:Eu@N_2 prepared in N_2 atmosphere, one can deduce that the strong reducibility of carbon and H_2/N_2 flowing

atmosphere at high temperatures leads to the formation of V_O. The formation of similar oxygen defects induced by treatments under reducing atmosphere were also observed for other phosphors such as $BaMgSiO_4$:Eu.[17] Paradoxically, the reducing atmosphere not only contributes to $Eu^{3+} \rightarrow Eu^{2+}$ conversion but also introduces oxygen defects simultaneously. With our material, this contradiction is skillfully solved by GeO_2 addition. O^{2-} ions can be introduced during GeO_2 decomposition by the following reaction: $2GeO_2$ (s) → 2GeO (s) + O_2 (g), and GeO (g) + H_2 (g) → Ge (s) + H_2O (g).[18] The O^{2-} ions from GeO_2 decomposition effectively compensate for the loss of oxygen ions, leading to the decrease of V_O (Figure 2e and Figure 1d). Moreover, the GeO_2 decomposition occurring at high temperatures will also lead to the formation of Ge metal (Figure S7a), suggesting that Ge^{4+} ions do not enter CaO host lattice. Thus, the cell volumes and bond lengths of [CaO_6] are maintained nearly unchanged with the increasing of GeO_2 amount (Figure S7b). This view is further confirmed by the Ge3*d* XPS spectrum (Figure S8a), elemental mapping images (Figure S8b) and DFT calculations (Table S3). The details of the Rietveld refinements for CaO:Eu@C+*x*GeO_2 (*x* = 0-8%) samples are exhibited in Figure S9, S10 and Table S4-7.

Based on the above results, a simplified schematic (**Figure 2**f) was drawn to explain the mechanism of TQ. The bandgap of CaO was predicted to be 3.97 eV by DFT calculation, close to the measured value (3.86 eV). The removal of O atom creates a defect energy level (V_O~2.36 eV) within the bandgap (Figure 2d). Under 470 nm excitation (2.63 eV), the electrons are promoted to 5*d* band, and then emits in the NIR region after a Stokes shift. When the temperature increases, electrons partly transfer to conduction band (CB) and cause TQ [process (1)]. Some electrons will be captured by the oxygen defect levels and then thermally ionized to CB under electron-phonon interaction [process (2)]. As for CaO:Eu@C+4%GeO_2 sample, the TQ process (2) was effectively suppressed due to the decrease of defect concentration, thus leading to the excellent thermal stability and long decay time. Not only GeO_2 discussed here but also SnO_2 have a similar positive effect on the

improvement of emission intensity and thermal stability of CaO:Eu. As depicted in the Figure S11, all the XRD patterns of SnO_2 treated samples are well indexed to the CaO phase, and the emission intensity of CaO:Eu@C+1.5%SnO_2 was enhanced about 1.6 times comparing to the PL intensity of CaO:Eu@C. Moreover, about 84% of the NIR emission at room temperature can be maintained at 125 °C. Therefore, such a method utilizing the characteristics of GeO_2 and SnO_2 decomposition during a high temperature reduction atmosphere can be generally adopted and it helps to optimize the thermal stability and the EQE of Eu^{2+}-activated phosphors.

The practical feasibility of high-performance CaO:Eu@C+4%GeO_2 phosphor for photon conversion in broadband NIR light sources has been tested and realized based on a commercial blue LED (455 nm) chip. **Figure 3**a shows the emission spectra of the fabricated NIR-LED under different drive currents in the range of 20-300 mA. The emission peaks are stable and the intensity grows continuously with the increase of the drive currents. To evaluate the performance of the CaO:Eu@C+4%GeO_2 phosphor in the NIR LED light source, the electricity-to-NIR power conversion, the electricity-to-blue power conversion and NIR output power were achieved and shown in **Figure 3**b. When the drive current increases from 20 to 300 mA, the NIR output power raises from 70 to 766 mW, while the electricity-to-NIR efficiency gradually decreases due to the "efficiency droop" of the InGaN blue chip. In particular, the NIR output power and photoelectric efficiency under current of 100 mA (319.5 mW@23.4%) and 300 mA (766.1 mW@17.1%) are the highest values reported so far, as exhibited in the comparison in Table S1. To highlight the application prospect of high-efficiency and thermally stable CaO:Eu@C+4%GeO_2 phosphor in the field of night vision, sapphire, UV adhesives, beam homogenizer, condenser and four high-power blue LEDs (455 nm, 10 W) were used to fabricate a high-power NIR light device. A 5.2 W NIR light source was obtained (Figure S12 and **Figure 3**c). Landscape photography taken with ordinary cameras in the daytime are clear (**Figure 3**d), but neither visible light cameras nor NIR

cameras can capture clear photos in a dark night (**Figure 3**e). In contrast, with the aid of the as-prepared NIR light source, a clear black-and-white photo of the pavilion at a distance of 65 meters was successfully taken by using the same near-infrared camera (**Figure 3**f). These results demonstrate that CaO:Eu@C+4%GeO_2 phosphor with high luminous efficiency and thermal stability can be successfully used for high-power NIR light sources.

3. Conclusion

In summary, the external quantum efficiency and thermal resistance of europium activated calcium oxide phosphor have been greatly improved and reach record values. The carbon paper wrapping strategy contributed to optimize the formation of Eu^{2+} centers leading to high quantum efficiency. In parallel, the O^{2-} ions formed *in-situ* from GeO_2 decomposition further decrease the concentration of oxygen vacancies, and result in the improvement of thermal stability from 57% to 90% at 125 °C. High EQE (54.7%) and photoelectric efficiency (100 mA@23.4%) make it possible to be used in high-power NIR devices. The general effect observed in SnO_2 treated samples certified the universality and effectiveness of this strategy. Our work will motivate future research on optimizing the luminescent properties of doped solid-state phosphors, showcasing the potential of this strategy in high-power broadband NIR devices.

Experimental Section/Methods

Materials and Preparation: CaO:Eu and CaO:Eu@C+*x*GeO_2 phosphors were synthesized by the traditional high temperature solid state reaction method. $CaCO_3$ (99.99%), Eu_2O_3 (99.99%) and GeO_2 (99.99%) were used as starting materials and weighed, grounded in stoichiometric proportions. Then the mixture was divided into two parts, and one part transferred into an alumina crucible directly, another part wrapped with carbon paper or place in graphite crucible. Subsequently, the powders were sintered at 1400 °C for 6 h in a

80%N_2/20%H_2 atmosphere. After cooling down naturally to room temperature, the products were reground into fine powders for further investigations.

Characterization: X-ray powder diffraction (XRD) patterns were measured in the range of 5^o-120^o on a D8 Advance X-ray diffractometer (XRD, Bruker Corporation, Germany). The structure refinement was performed by TOPAS 4.2 software.[19] The photoluminescence (PL), photoluminescence excitation (PLE) spectra and quantum efficiency (QE) were measured by a FL1000 fluorescence spectrophotometer (Edinburgh Instruments, UK) with visible and NIR PMT detectors. The temperature-dependent spectra and decay curves were also collected by FL1000 equipped with a temperature control instrument (OXFORD) and a 450 nm pulse laser diode, respectively. The diffuse reflectance spectra were recorded on a Hitachi UH4150 UV-vis-NIR spectrophotometer. The morphology and microstructure of phosphors were investigated using a field-emission scanning electron microscope (SEM, JEOL JSM-6510A). Thermoluminescence (TL) spectra were measured using a TOSL-3DS instrument (Ai-di-rui-sheng Company, China) equipped with a Hg lamp as the UV radiation source. Electron paramagnetic resonance (EPR) spectra were measured at room temperature using an EMXplus X-band spectrometer (Bruker, Germany). X-ray photoelectron spectroscopy (XPS) spectra were recorded by a VG ESCALABMK II electron spectrometer with a Mg Kα (1200 eV) line as an excitation source.

WLED Fabrication: The low-power NIR pc-LEDs were fabricated by encapsulating the mixture of CaO:Eu@C+4%GeO_2 phosphor and transparent epoxy resin on blue (455 nm, 3 W) LED Chips. The emission spectra and photoelectric properties of the fabricated pc-LEDs were collected by a NOVA Laboratory Class Spectrometer equipped with Morpho 3.2 software. For high-power NIR LED application, the mixture of CaO:Eu@C+GeO_2 phosphor and transparent epoxy resin was firstly coated on the surface of sapphire, then the sapphire were fixed onto four high-power blue LED (455 nm, 10 W). The photoelectric properties of

the fabricated high-power NIR LED were measured on an integrating sphere spectroradiometer system (ATA-1000, Ever fine).

Computational method: In order to study the structure well, we used the Vienna ab initio simulation package (VASP) codes to calculate the lattice structure and electronic structure of CaO based on the density functional theory (DFT).[20] The generalized gradient approximation with the Perdew-Burke-Ernzerhof functional was employed as the exchange-correlation potential. To evaluate the Ge, V_{Ca} and V_O distribution in GaO, a 2 × 2 × 2 CaO supercell was adopted. The cut-off energy E_{cut} of 400 eV was used throughout all the calculations. A gamma-centered 4 × 4 × 4 k-mesh grid in the Brillouin zone was applied to determine the self-consistent charge density using the Monkhorst–Packscheme. The crystal lattice was fully relaxed until the atomic force was less than 0.02 eV $Å^{-1}$. The energy convergence criterion for self-consistent electronic calculation was set to 1.0×10^{-5} eV/atom.

Supporting Information

Supporting Information is available from the Wiley Online Library or from the author.

Acknowledgements

This research was supported by the National Key Research and Development Program of China (2021YFB3500400 and 2021YFE0105700), National Natural Science Foundations of China (Grant No. 52102169, 51972118 and 51961145101), Guangzhou Science & Technology Project (202007020005), China Postdoctoral Science Foundation (2021M691053), the State Key Laboratory of Luminescent Materials and Devices (Skllmd-2021-09). This work is also funded by Young Elite Scientists Sponsorship Program by China Association for Science and Technology No. YESS20200053).

Conflict of Interest

The authors declare no conflict of interest.

Received: ((will be filled in by the editorial staff))

Revised: ((will be filled in by the editorial staff))

Published online: ((will be filled in by the editorial staff))

References

[1] a) M. Vasilopoulou, A. Fakharuddin, F. P. García de Arquer, D. G. Georgiadou, H. Kim, A. R. b. Mohd Yusoff, F. Gao, M. K. Nazeeruddin, H. J. Bolink, E. H. Sargent, *Nat. Photon.* **2021**, *15*, 656; b) Y. Gu, Z. Guo, W. Yuan, M. Kong, Y. Liu, Y. Liu, Y. Gao, W. Feng, F. Wang, J. Zhou, D. Jin, F. Li, *Nat. Photon.* **2019**, *13*, 525; c) K. Klaue, W. Han, P. Liesfeld, F. Berger, Y. Garmshausen, S. Hecht, *J. Am. Chem. Soc.* **2020**, *142*, 11857; d) J. J. Joos, D. Van der Heggen, L. Martin, L. Amidani, P. F. Smet, Z. Barandiaran, L. Seijo, *Nat. Commun.* **2020**, *11*, 3647; e) C. Ding, Y. Huang, Z. Shen, X. Chen, *Adv. Mater.* **2021**, *33*, e2007768; f) V. Rajendran, M. H. Fang, W. T. Huang, N. Majewska, T. Lesniewski, S. Mahlik, G. Leniec, S. M. Kaczmarek, W. K. Pang, V. K. Peterson, K. M. Lu, H. Chang, R. S. Liu, *J. Am. Chem. Soc.* **2021**, *143*, 19058.

[2] a) K. Tuong Ly, R.-W. Chen-Cheng, H.-W. Lin, Y.-J. Shiau, S.-H. Liu, P.-T. Chou, C.-S. Tsao, Y.-C. Huang, Y. Chi, *Nat. Photon.* **2016**, *11*, 63; b) X. Gong, Z. Yang, G. Walters, R. Comin, Z. Ning, E. Beauregard, V. Adinolfi, O. Voznyy, E. H. Sargent, *Nat. Photon.* **2016**, *10*, 253; c) N. Tessler, V. Medvedev, M. Kazes, S. Kan, U. Banin, *Science* **2002**, *295*, 1506; d) B. Su, M. Li, E. Song, Z. Xia, *Adv. Funct. Mater.* **2021**, *31*, 2105316.

[3] R.-J. Xie, *Light Sci. Appl.* **2020**, *9*, 155.

[4] E. Song, X. Jiang, Y. Zhou, Z. Lin, S. Ye, Z. Xia, Q. Zhang, *Adv. Opt. Mater.* **2019**, *7*, 1901105.

[5] a) Z. Jia, C. Yuan, Y. Liu, X. J. Wang, P. Sun, L. Wang, H. Jiang, J. Jiang, *Light Sci. Appl.* **2020**, *9*, 86; b) F. He, E. Song, Y. Zhou, H. Ming, Z. Chen, J. Wu, P. Shao, X. Yang, Z. Xia, Q. Zhang, *Adv. Funct. Mater.* **2021**, *31*, 2103743.

[6] S. Liu, H. Cai, S. Zhang, Z. Song, Z. Xia, Q. Liu, *Mater. Chem. Front.* **2021**, *5*, 3841.

[7] a) Y. H. Kim, P. Arunkumar, B. Y. Kim, S. Unithrattil, E. Kim, S.-H. Moon, J. Y. Hyun, K. H. Kim, D. Lee, J.-S. Lee, W. B. Im, *Nat. Mater.* **2017**, *16*, 543; b) P. Pust, V. Weiler, C. Hecht, A. Tucks, A. S. Wochnik, A. K. Henss, D. Wiechert, C. Scheu, P. J. Schmidt, W. Schnick, *Nat. Mater.* **2014**, *13*, 891.

[8] a) J. Qiao, G. Zhou, Y. Zhou, Q. Zhang, Z. Xia, *Nat. Commun.* **2019**, *10*, 5267; b) Z. Yang, Y. Zhao, Y. Zhou, J. Qiao, Y. C. Chuang, M. S. Molokeev, Z. Xia, *Adv. Funct. Mater.* **2021**, DOI: 10.1002/adfm.2021039272103927.

[9] S. Li, L. Wang, D. Tang, Y. Cho, X. Liu, X. Zhou, L. Lu, L. Zhang, T. Takeda, N. Hirosaki, R.-J. Xie, *Chem. Mater.* **2017**, *30*, 494.

[10] a) H. Liu, Z. Xia, J. Zhuang, Z. Zhang, L. Liao, *J. Phys. Chem. Solids* **2012**, *73*, 104; b) C.-Y. Wang, R.-J. Xie, F. Li, X. Xu, *J. Mater. Chem. C* **2014**, *2*, 2735; c) J. Qiao, L. Ning, M. S. Molokeev, Y. C. Chuang, Q. Liu, Z. Xia, *J. Am. Chem. Soc.* **2018**, *140*, 9730.
[11] N. Yamashita, *J. Electroc. Soc.* **1993**, *140*, 840.
[12] C. R. Ronda, *Luminescence: from theory to applications*, John Wiley & Sons, **2007**.
[13] J. Qiao, M. Amachraa, M. Molokeev, Y.-C. Chuang, S. P. Ong, Q. Zhang, Z. Xia, *Chem. Mater.* **2019**, *31*, 7770.
[14] P. Dorenbos, *J. Phys. Condens. Matter.* **2005**, *17*, 8103.
[15] M. Zhao, H. Liao, L. Ning, Q. Zhang, Q. Liu, Z. Xia, *Adv. Mater.* **2018**, *30*, 1802489.
[16] A. Jagannatha Reddy, M. K. Kokila, H. Nagabhushana, J. L. Rao, C. Shivakumara, B. M. Nagabhushana, R. P. Chakradhar, *Spectrochim. Acta A* **2011**, *81*, 59.
[17] W. Ji, M. H. Lee, L. Hao, X. Xu, S. Agathopoulos, D. Zheng, C. Fang, *Inorg. Chem.* **2015**, *54*, 1556.
[18] a) M. M. Jumidali, M. R. Hashim, *Superlattice. Microst.* **2012**, *52*, 33; b) T. Yokokawa, M. Koizumi, M. Shimoji, K. Niwa, *J. Am. Chem. Soc.* **1957**, *79*, 3365.
[19] V. TOPAS, **Bruker AXS: Karlsruhe, Germany, 2008**.
[20] a) G. Kresse, J. Furthmüller, *Phys. Rev. B* **1996**, *54*, 11169; b) G. Kresse, D. Joubert, *Phys. Rev. B* **1999**, *59*, 1758.

Figures

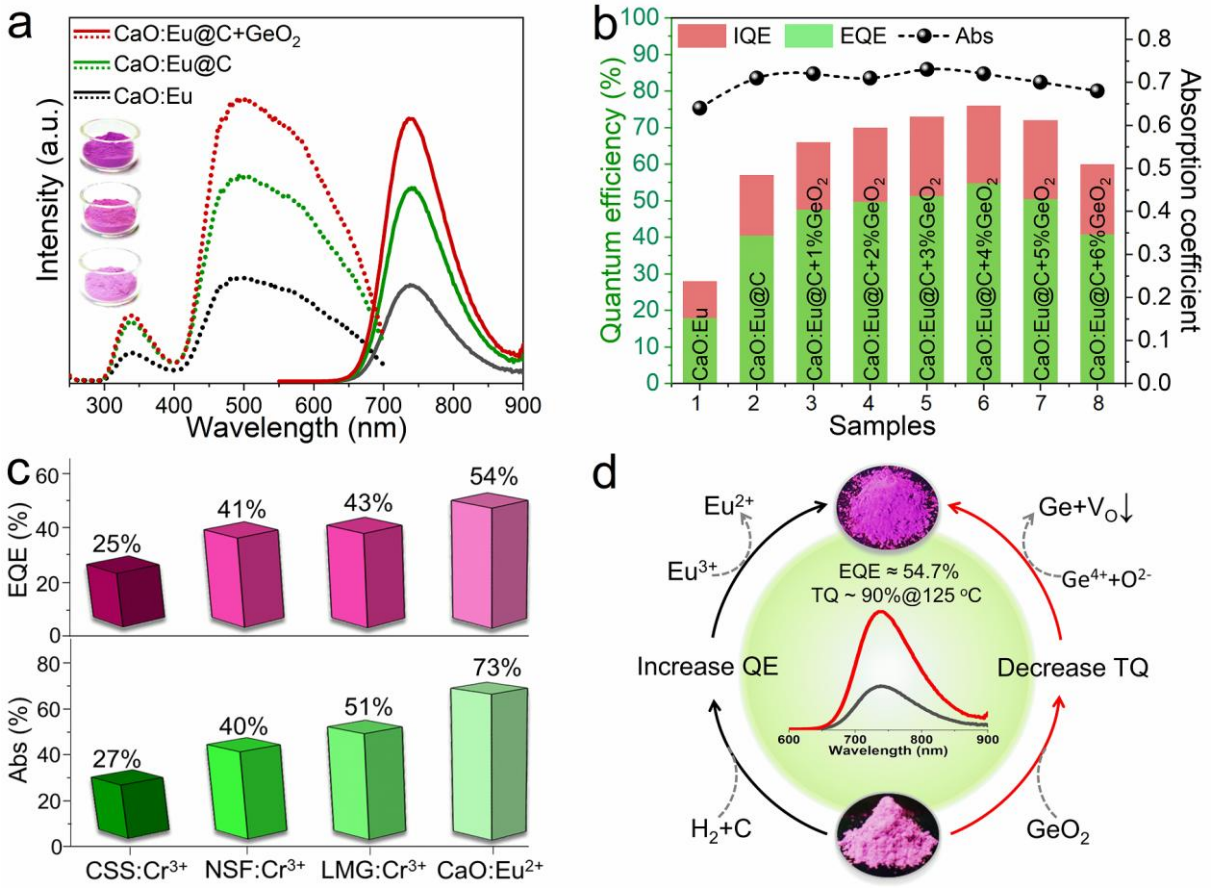

Figure 1 Photoluminescence properties of europium-activated calcium oxide phosphors. a) Excitation, emission spectra and photographs of CaO:Eu, CaO:Eu@C and CaO:Eu@C+GeO_2 phosphors. b**)** The internal/external quantum efficiency (IQE, EQE) and absorption efficiency of CaO:Eu@C+*x*GeO_2 phosphors (*x* = 0-6%). c) Comparison of EQE and absorption efficiency of CaO:Eu@C+4%GeO_2 with the excellent NIR phosphors reported so far including $Ca_3Sc_2Si_3O_{12}:Cr^{3+}$ (CSS:Cr^{3+}), $Na_3ScF_6:Cr^{3+}$ (NSF:Cr^{3+}), $LaMgGa_{11}O_{19}:Cr^{3+}$ (LMG:Cr^{3+}). d) Schematic illustration for the enhancement of luminescence and thermal stability of europium-activated calcium oxide phosphor.

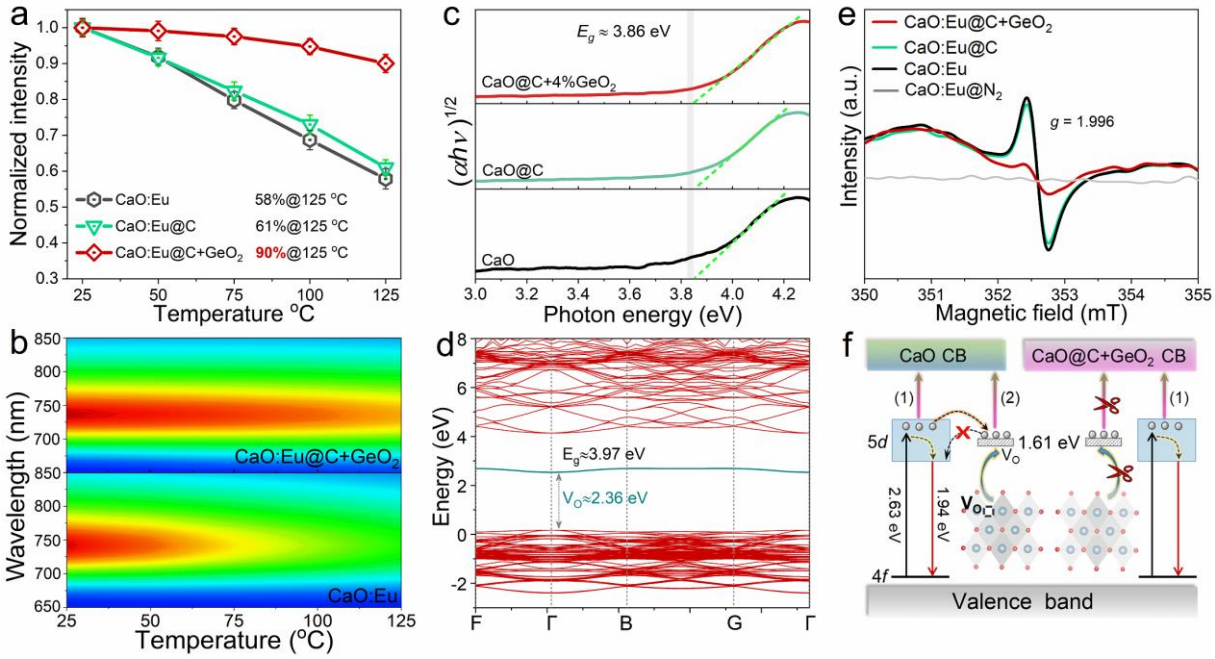

Figure 2 Thermal quenching property of CaO:Eu@C+GeO_2 phosphor. a) Temperature dependence of the relative integrated photoluminescence intensity for CaO:Eu, CaO:Eu@C and CaO:Eu@C+GeO_2 phosphor. b) Temperature dependence of the spectral emission. c) The calculated energy gap by Tauc equation for each samples. d) Electronic band structure of CaO and the calculated defect levels of V_O. e) EPR spectra of CaO:Eu, CaO:Eu@C and CaO:Eu@C+GeO_2 compounds. f) Schematic illustration of the mechanism of the thermal quenching process of the CaO:Eu and CaO:Eu@C+GeO_2 phosphor.

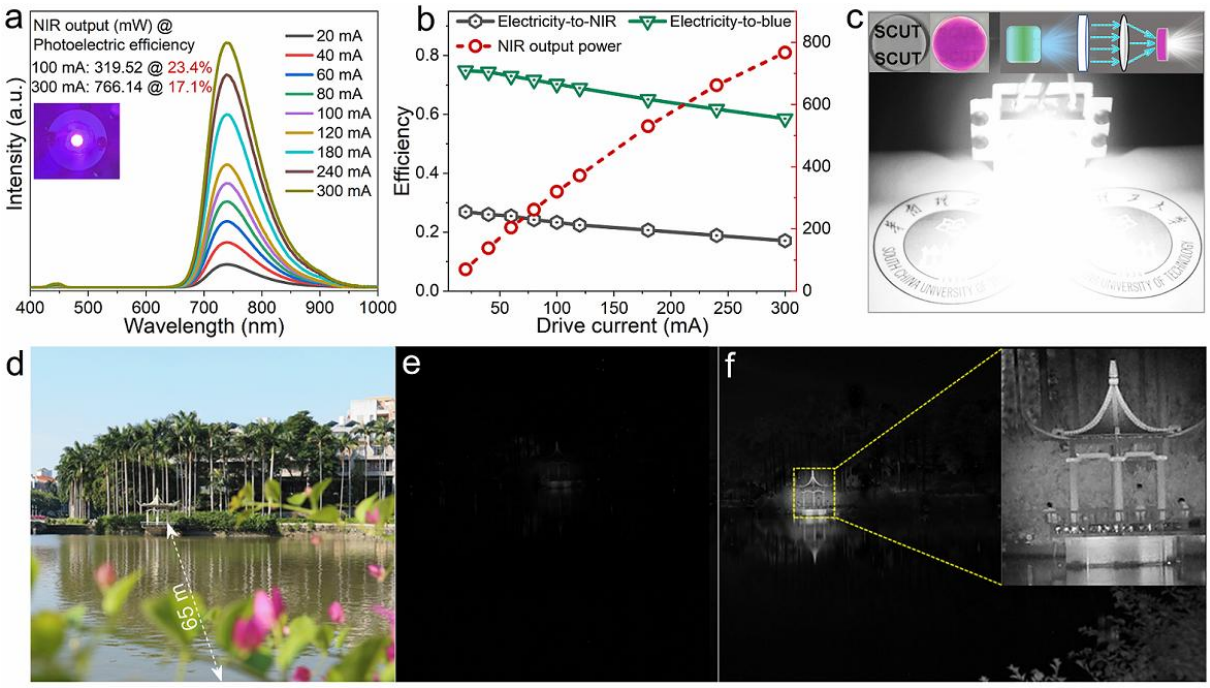

Figure 3 NIR performance and application of CaO:Eu@C+GeO_2 phosphor based LEDs device. a) Photoluminescence spectra and photographs of as-fabricated NIR-LED by combining a commercial blue LED and CaO:Eu@C+GeO_2 phosphor. b) NIR output power, electricity-to-blue light and electricity-to-NIR light power conversion efficiency under various drive current. c) Photographs and schematic illustration of high-power NIR-LED device by combining the blue LEDs and phosphor-sapphire composite. d-e) Photographs of pavilion captured by visible camera at day and (e) night. f) Photograph of pavilion captured by NIR camera under the illumination of the fabricated high-power NIR-LED device.

Here we report how the photoluminescence quantum efficiency of CaO:Eu NIR phosphor was significantly improved and stabilized. By utilizing GeO_2 decomposition, the oxygen vacancies in the CaO lattice were effectively repaired. A record high EQE of 54.7% at 740 nm is obtained with a thermal stability greatly improved from 57% to 90% at 125 °C.

Keywords: near-infrared luminescence, phosphor, light-emitting diodes

*Jianwei Qiao, Shuai Zhang, Xinquan Zhou, Weibin Chen, Romain Gautier, Zhiguo Xia**

Near-infrared light-emitting diode utilizing europium-activated calcium oxide phosphor with external quantum efficiency of up to 54.7%

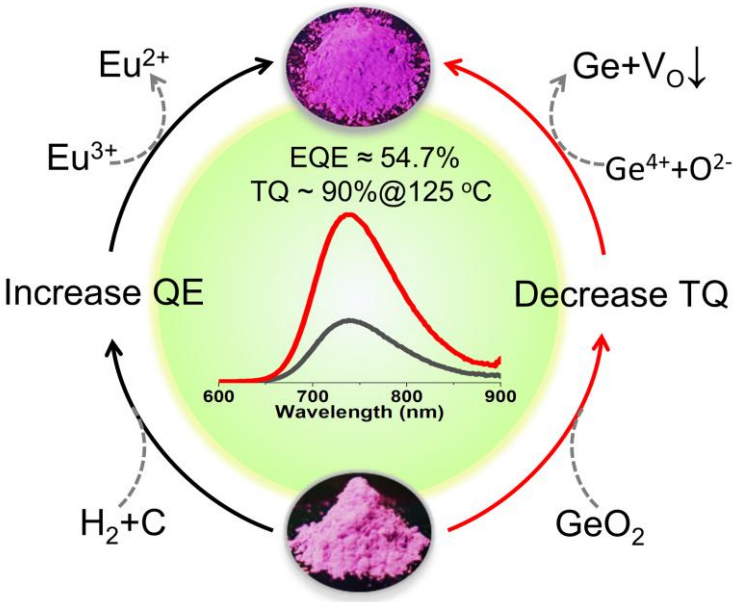

TOC

Supporting Information

Near-infrared light-emitting diode utilizing europium-activated calcium oxide phosphor with external quantum efficiency of up to 54.7%

Jianwei Qiao, Shuai Zhang, Xinquan Zhou, Weibin Chen, Romain Gautier, Zhiguo Xia*

Table S1 The photoelectric properties of NIR pc-LED devices fabricated by relative NIR emission phosphors.

Phosphors	IQE/EQE	Current (mA)	NIR output @ photonic efficiency	Ref.
$CaO:Eu^{2+}$@C+GeO_2	76%/54.7%	100	319.5@23.4%	This work
		300	766.1@17.1%	
$K_3LuSi_2O_7:Eu^{2+}$	15%/-	100	21.5@7.1%	[1]
$MgAl_2O_4:Mn^{2+}$	53%/-	100	69.6@2.49%	[2]
$Gd_3Sc_{1.5}Al_{0.5}Ga_3O_{12}:Cr^{3+}$	90%/-	100	50@17%	[3]
$Ca_3Sc_2Si_3O_{12}:Cr^{3+}$	92.3%/25.5	520	109.9@3.8%	[4]
$Ca_{3-x}LuHf_2Al_{2+x}Si_{1-x}O_{12}:Cr^{3+}$	-/-	100	46.1@15.75%	[5]
$K_2NaScF_6:Cr^{3+}$	74%/-	100	193.9@14.02	[6]
$LiScP_2O_7:Cr^{3+}$, Yb^{3+}	74%/-	100	36@12%	[7]
$YAl_3(BO_3)_4:Cr^{3+}$	86.7%/-	100	50.6@17.4%	[8]
$Ga_{2-x}Sc_xO_3:Cr^{3+}$	99%/-	350	66.1@6.57%	[9]
$BaMgAl_{10}O_{17}:Cr^{3+}$	94%/-	100	3.4@3.4%	[10]
$ScF_3:Cr^{3+}$	45%/-	100	8.5@3%	[11]
$LiGaP_2O_7:Cr^{3+}$	47.8%/28.3	120	28.1@7.8%	[12]
$LaMgGa_{11}O_{19}:Cr^{3+}$	82.6%/42.5	--	--	[13]
$SrGa_{12}O_{19}:Cr^{3+}$	98.2/45%	--	--	[13]
$Na_3ScF_6:Cr^{3+}$	91.5%/40.8	100	291.1@20.94	[14]
		300	698.7@15.46	

Table S2 Luminescent decay times (τ_1, τ_2) and the fitting constants (A_1, A_2) of the fast and slow components and average decay times (τ_{av}). These decay times were measured by FLS1000 equipped with 450 nm pulse laser diode as excitation. All the datas were fitted by exponential curve fitting.

sample	A_1	τ_1	A_2	τ_2	τ_{av} (μs)	R^2_{adj}
CaO:Eu	8711.98	0.83	1688.94	0.15	0.80	0.9997
CaO:Eu@C	9518.37	1.02	1311.21	0.27	0.99	0.9998
CaO:Eu@C+0.02GeO_2	9003.29	1.05	1273.39	2.65	1.47	0.9997

Average decay times are calculated by the following question:

$$\tau_{av} = \frac{A_1\tau_1^2 + A_1\tau_2^2}{A_1\tau_1 + A_2\tau_2}$$

Where A_1 and A_2 are the corresponding fitting constants; τ_1, τ_2 are lifetimes for the fast and slow components.

Table S3 The formation energy calculated by DFT.

	Formation energy (eV)
$Ca_{30}GeO_{32}$	8.74
$Ca_{32}O_{32}$	0
Ca-defect	5.69
O-defect	-3.27

The formation energies for each model were calculated using the following formula:[15]

$$E^f[X^q] = E_{tot}[X^q] - E_{tot}[bulk] - \sum_i n_i\mu_i + qE_F$$

where $E_{tot}[X^q]$ is the total energy derived from a supercell calculation containing the defect X, and $E_{tot}[bulk]$ is the total energy for the perfect crystal using an equivalent supercell. The integer n_i indicates the number of atoms of type i (host atoms or impurity atoms) that have been added to ($n_i > 0$) or removed from ($n_i < 0$) the supercell to form the defect, and the μ_i are the corresponding chemical potentials of these species.

Note: DFT calculations revealed that Ge^{4+} can hardly to substitute Ca sites, because of the formation energies is about 8.74 eV higher than that of the initial model. Moreover, oxygen vacancy is easy to form with a negative formation energy -3.27 eV, while the defect V_{Ca} can be hardly generated with a formation energy of 5.69 eV.

Table S4 Main parameters of processing and refinement of the CaO:0.15%Eu, *x*GeO_2 samples.

x(Ge)	Space Group	Cell parameters (Å), Cell Volume (Å^3)	R_{wp}, R_p, R_{exp}, χ^2
0	Fm-3m	a = 4.8129(2) β = 90.0000 V = 111.4834(9)	8.25, 6.04, 4.43, 3.47
0.02	Fm-3m	a = 4.8138(20) β = 90.0000 V = 111.5512(8)	6.92, 5.05, 4.42, 2.45
0.04	Fm-3m	a = 4.81151(2) β = 90.0000 V = 111.3895(8)	7.20, 5.38, 4.41, 2.66
0.06	Fm-3m	a = 4.8131(8) β = 90.0000 V = 111.4970(3)	7.20, 5.17, 4.52, 2.53
0.08	Fm-3m	a = 4.8113(3) β = 90.0000 V = 111.3746(11)	7.04, 5.02, 4.40, 2.57

Table S5 Fractional atomic coordinates and isotropic displacement parameters (Å^2) of CaO:0.15%Eu, *x*GeO_2.

Atom	*x*	*y*	*z*	B_{iso}	*Occ.*
x = 0					
Ca	0.0000	0.0000	0.0000	0.005(23)	1
O	0.5000	0.5000	0.5000	0.223(52)	1
x = 0.02					
Ca	0.0000	0.0000	0.0000	0.315(17)	1
O	0.5000	0.5000	0.5000	0.516(41)	1
x = 0.04					
Ca	0.0000	0.0000	0.0000	0.204(18)	1
O	0.5000	0.5000	0.5000	0.291(42)	1
x = 0.06					
Ca	0.0000	0.0000	0.0000	0.552(15)	1
O	0.5000	0.5000	0.5000	0.321(23)	1
x = 0.08					
Ca	0.0000	0.0000	0.0000	0.593(15)	1
O	0.5000	0.5000	0.5000	0.452(32)	1

Table S6 Bond lengths (Å) of CaO:0.15%Eu, *x*GeO_2.

	x=0	*x* = 0.02	*x* = 0.04	*x* = 0.06	*x* = 0.08
Ca—O	2.4064(0)	2.4072(0)	2.4058(0)	2.4065(0)	2.4056(0)

Table S7 Main parameters of refinement for the CaO:0.15%Eu and CaO:0.15%Eu, 0.08GeO_2 samples based on the synchrotron XRD profiles.

x(GeO_2)	Space Group	Cell parameters (Å), Cell Volume (Å^3)	R_{wp}, R_p, R_{exp}
0	Fm-3m	*a* = 4.8122(0) *β* = 90.0000 *V* = 111.44(0)	2.39, 5.34, 4.65
0.08	Fm-3m	*a* = 4.8119(0) *β* = 90.0000 *V* = 111.42(0)	2.10, 4.78, 1.27

Note: In our work, the internal quantum efficiencies (IQE) and external quantum efficiencies (EQE) test were performed at room temperature by using a barium sulfate coated integrating sphere (150 mm in diameter) that attached to FL1000. The IQE and EQE were calculated by using the following equations:

$$\eta_{IQE} = \frac{\varepsilon}{\alpha} = \frac{\int L_S}{\int E_R - \int E_S}; \quad \eta_{EQE} = \frac{\varepsilon}{\alpha} = \frac{\int L_S}{\int E_R}; \quad \eta_{EQE} = \eta_{IQE} * Abs$$

where ε is the number of photons emitted by the sample, and α is the number of photons absorbed by the sample. L_S is the luminescence emission spectrum of the sample; E_S is the spectrum of the light used for exciting the sample; E_R is the spectrum of the excitation light without the sample in the sphere; Abs is absorption efficiency. Obviously, EQE is proportional to IQE and Abs.

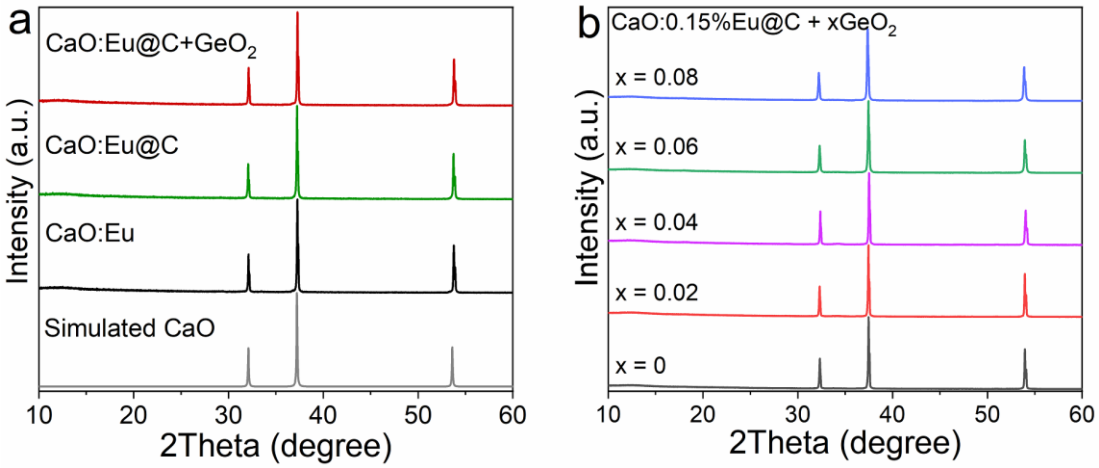

Figure S1 Structural characterization of CaO:Eu phosphor. a) X-ray powder diffraction patterns of CaO:Eu, CaO:Eu@C, CaO:Eu@C+GeO_2 and the calculated pattern based on Rietveld refinement data (gray line). b) XRD patterns of CaO:Eu, *x*GeO_2 (*x* = 0-8%) samples.

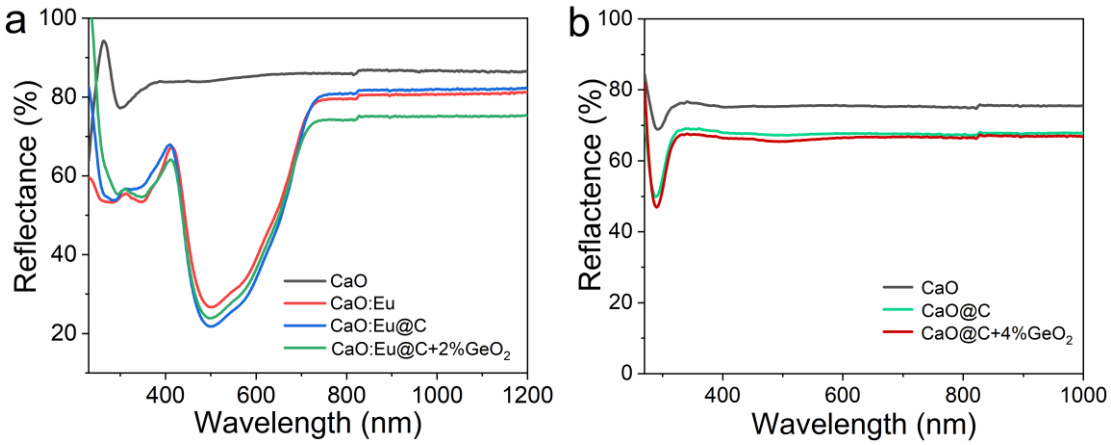

Figure S2 a) UV-vis diffuse reflectance spectra of CaO, CaO:Eu, CaO:Eu@C and CaO:Eu@C+4%GeO_2. powder. b) UV-vis diffuse reflectance spectra of CaO, CaO@C and CaO@C+GeO_2 host.

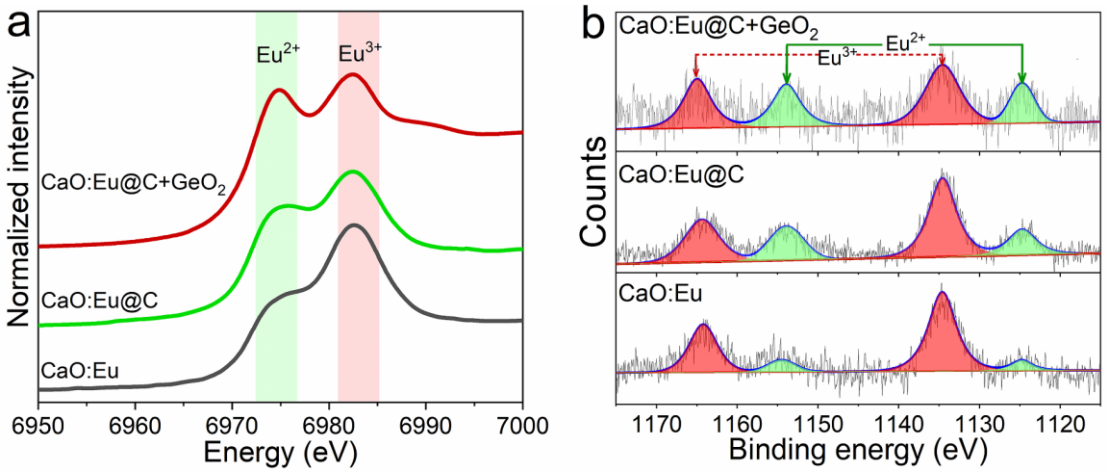

Figure S3 a) XANES spectra of the Eu L3 edge for CaO:Eu, CaO:Eu@C and CaO:Eu@C+GeO_2 samples. b) XPS spectra of Eu3*d* region recorded for CaO:Eu, CaO:Eu@C and CaO:Eu@C+GeO_2 samples.

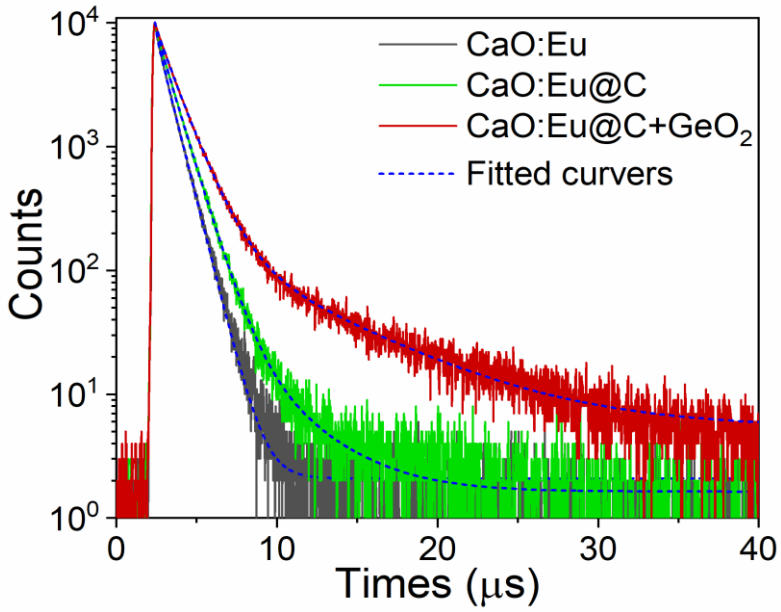

Figure S4 Photoluminescence decay curves of the different phosphors under 450 nm pulse laser diode excitation. The statistical photons are 10000. All the datas were fitted by the FAST software attached with FL1000.

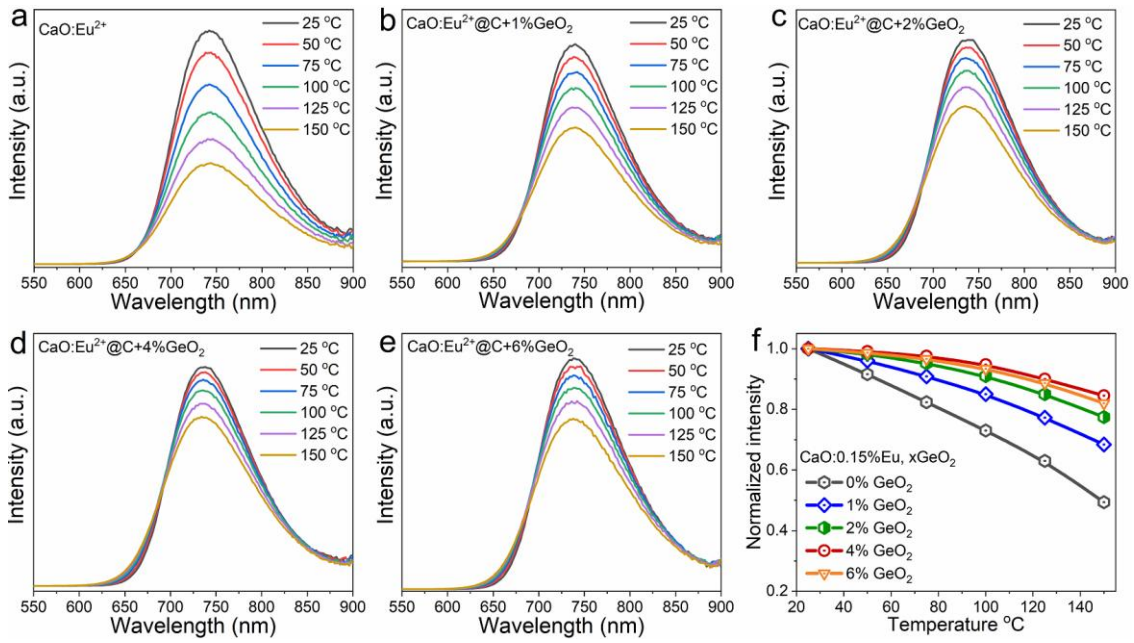

Figure S5 a-e) Temperature-dependent emission spectra of CaO:Eu@C+xGeO$_2$ (x = 0 -6%) phosphor under 470 nm excitation in the temperature range 25-150 ^{o}C with a temperature interval of 25 ^{o}C. f) Temperature dependence of the relative integrated photoluminescence intensity for CaO:Eu@C+xGeO$_2$.

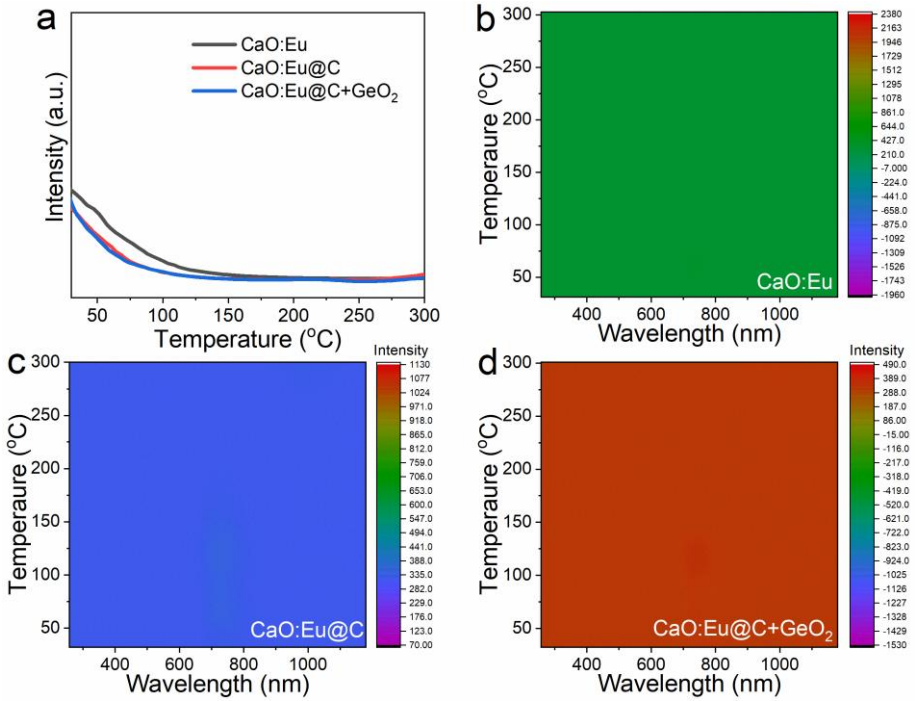

Figure S6 a) Thermoluminescence curves of CaO:Eu, CaO:Eu@C and CaO:Eu@C+4%GeO$_2$ in the temperature range 25-300 ^{o}C. b-d) 3D- thermoluminescence spectra of CaO:Eu, CaO:Eu@C and CaO:Eu@C+4%GeO$_2$ after 254, 395 and 450 nm irradiation for 100 s at room temperature.

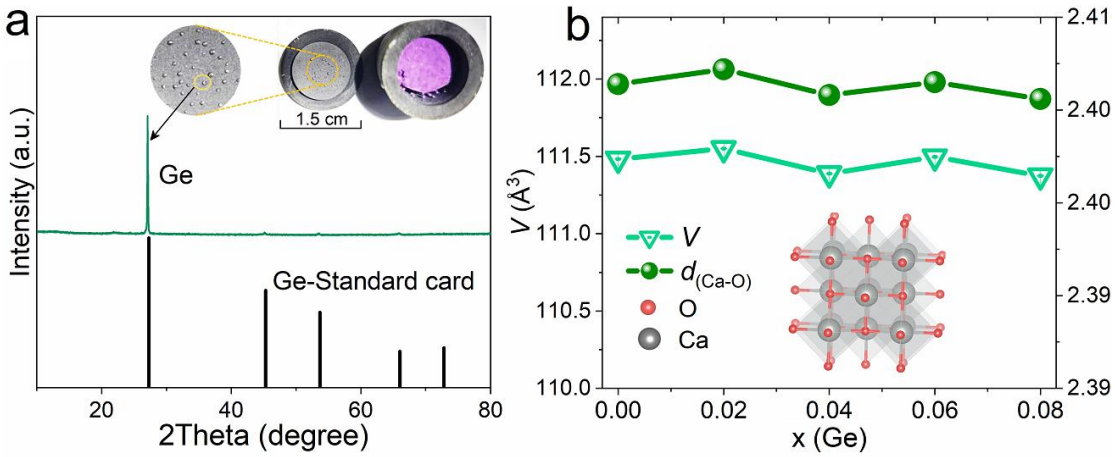

Figure S7 a) XRD diffraction patterns of compounds volatilized and adhered to the surface of graphite crucible during sintering process of CaO:Eu@C+8%GeO_2 sample. b) Cell volume $V(x)$ and average bond length d(Ca-O) dependence of the GeO_2 doping concentration (x = 0-0.08); the inset shows crystal structure of CaO:Eu, where gray and red spheres represent calcium and oxygen ions respectively. Note: The GeO_2 decompose into Ge metal under high temperature and reducing atmosphere, and deposited on the crucible wall and lid, suggesting that Ge^{4+} ions do not enter CaO host lattice.

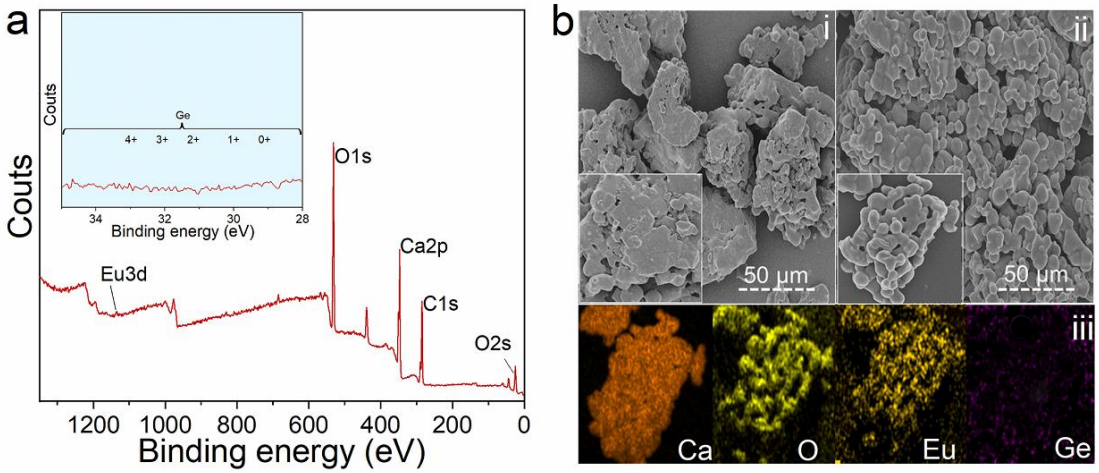

Figure S8 a) XPS spectra of CaO:Eu, 4%GeO_2. b) SEM images of CaO:Eu@C (i) and CaO:Eu@C+4%GeO_2 (ii) particles; and (iii) the element mapping images of Ca, O, Eu, and Ge for the selected particle.

Note: There are no XPS spectra peaks observed in the region from 26 to 35 eV, suggesting that no Ge^{4+}, Ge^{3+}, Ge^{2+}, Ge^{1+} and Ge^{0+} existed in CaO:Eu, 4%GeO_2 phosphor. Comparing with the scanning electron microscopy (SEM) images of the CaO:Eu@C (i), the surface and size of CaO:Eu@C+4%GeO_2 microcrystals become more smoother and uniform after doping GeO_2. This optimization in morphology is related to the decomposition of GeO_2 and the newly introduced O^{2-} ions. The elemental mapping images reveal that Ca, O, Eu element homogeneously dispersed within phosphor particles, while nearly no Ge element was observed. These results combined with the DFT calculations and XRD analysis suggest that Ge element did not enter the host lattice.

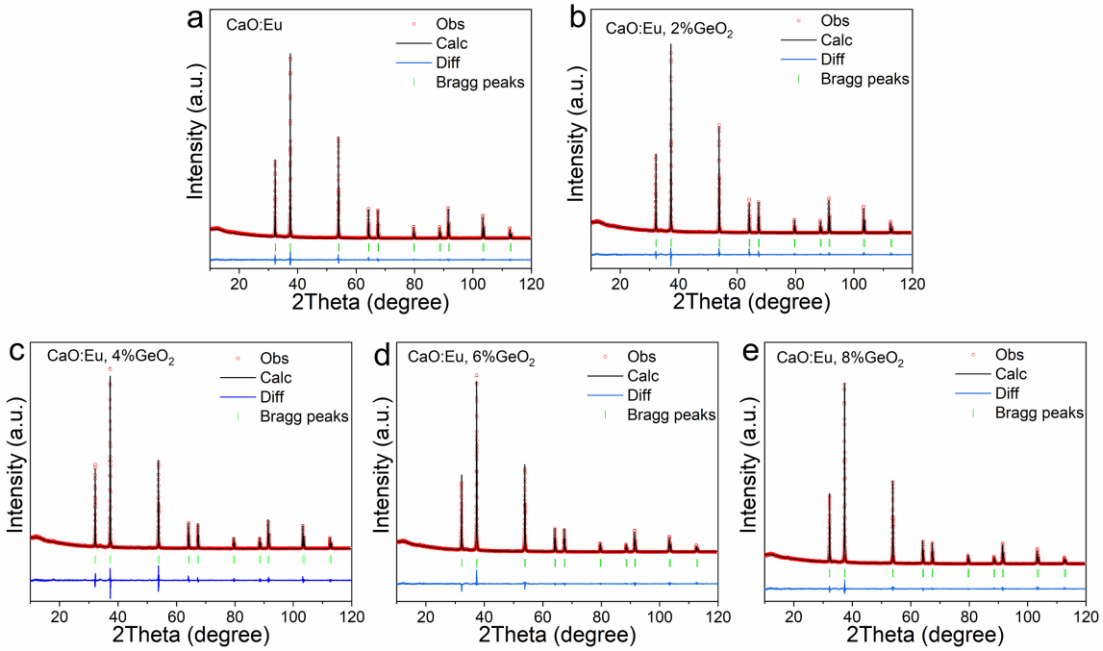

Figure S9 a-e) Rietveld refinements of CaO:Eu, xGeO$_2$ samples: x = 0-8% based on XRD datas.

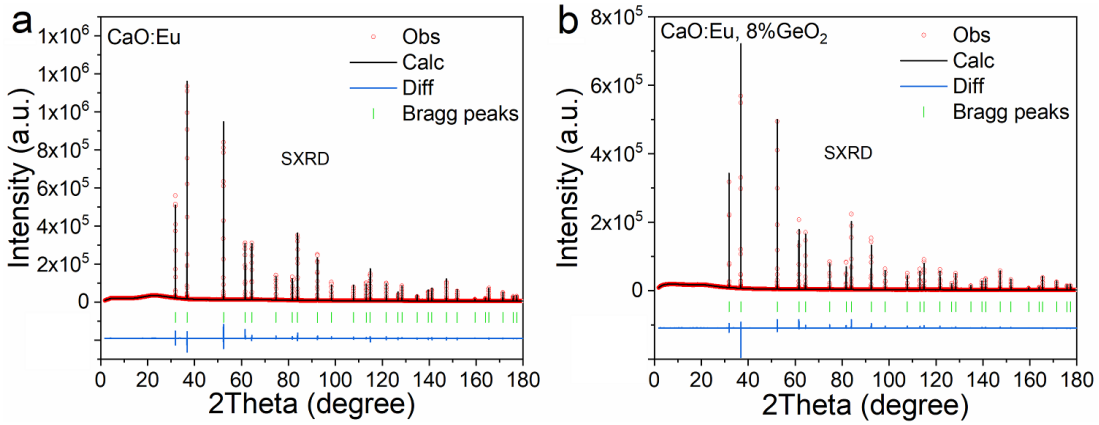

Figure S10 a-b) Rietveld refinement of the synchrotron XRD profile for CaO:Eu and CaO:Eu, 8%GeO$_2$.

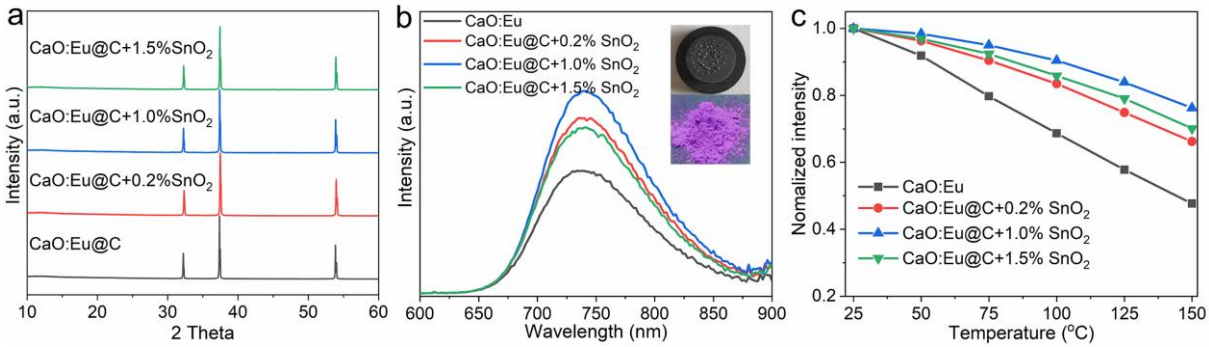

Figure S11 a) XRD patterns of CaO:Eu@C+xSnO$_2$ (x = 0-1.5%) phosphor. b) PL spectra of CaO:Eu@C+ xSnO$_2$ under 470 nm excitation, and the photographs of crucible lid and CaO:Eu@C+SnO$_2$ phosphor. c) Temperature-dependent emission spectra of CaO:Eu@C+ xSnO$_2$ phosphor in the temperature range 25-150 ^{o}C. Note: Similar Sn particles observed on the crucible lid suggests that Sn do not enter CaO host lattice.

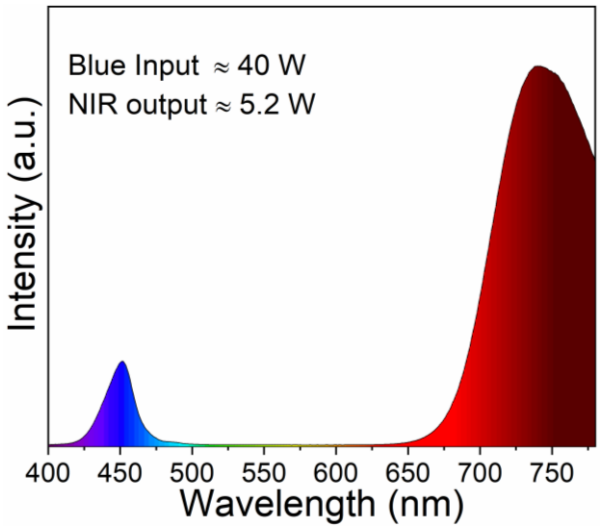

Figure S12 PL spectra of the fabricated high-power NIR-LED based on four InGaN chips (460 nm, 10 W) and CaO:Eu@C+4%GeO$_2$ phosphor.

Note: (1) The Eu dopant concentration is about 0.2 % for all samples mentioned in the article. With the increase of the Eu_2O_3 dopant concentration, the emission intensity increases and reaches a maximum at x = 0.2%, and then decreases due to the concentration quenching, as shown in the following figure. Thus, the optimal dopant concentration of Eu is about 0.2 %.

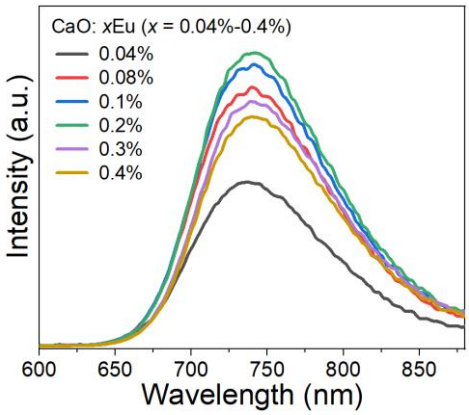

Figure S13. PL spectra of CaO:*x*Eu (x = 0.04%-0.4%) under 470 nm excitation.

Note: (2) CaO is hygroscopic and commonly known as quick lime. To evaluate the robustness of samples to air and moisture, CaO:Eu was exposed to the 85% relative humidity (RH) and 85 ° C for different times. As shown in **Figure S14**, the emission intensities decrease over times, and remain about 42.6% of the pristine sample after 240 min. Thus, the chemical stabilities of CaO:Eu phosphors are relatively poor. It needs to be further improved in the future works by the surface coating or LED packaging technology.

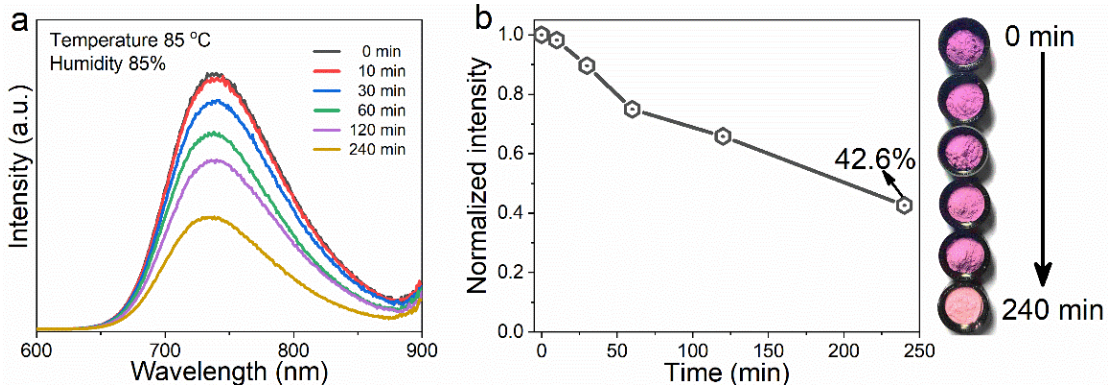

Figure S14. a) The PL spectra of the pristine CaO:Eu and samples treated in degradation conditions at 85% relative humidity (RH), 85 °C for different time, respectively. b) The normalized integrate PL intensities dependent on times and photographs of these samples under natural light.

Supplementary References

[1] J. Qiao, G. Zhou, Y. Zhou, Q. Zhang, Z. Xia, *Nat. Commun.* **2019**, *10*, 5267.

[2] E. Song, X. Jiang, Y. Zhou, Z. Lin, S. Ye, Z. Xia, Q. Zhang, *Adv. Opt. Mater.* **2019**, *7*, 1901105.

[3] E. T. Basore, H. Wu, W. Xiao, G. Zheng, X. Liu, J. Qiu, *Adv. Opt. Mater.* **2021**, *9*, 2001660.

[4] Z. Jia, C. Yuan, Y. Liu, X. J. Wang, P. Sun, L. Wang, H. Jiang, J. Jiang, *Light Sci. Appl.* **2020**, *9*, 86.

[5] L. Zhang, D. Wang, Z. Hao, X. Zhang, G. h. Pan, H. Wu, J. Zhang, *Adv. Opt. Mater.* **2019**, DOI: 10.1002/adom.2019001851900185.

[6] E. Song, H. Ming, Y. Zhou, F. He, J. Wu, Z. Xia, Q. Zhang, *Laser Photonics Rev.* **2020**, DOI: 10.1002/lpor.2020004102000410.

[7] L. Yao, Q. Shao, S. Han, C. Liang, J. He, J. Jiang, *Chem. Mater.* **2020**, *32*, 2430.

[8] M. Shi, L. Yao, J. Xu, C. Liang, Y. Dong, Q. Shao, *J. Am. Ceram. Soc.* **2021**, *104*, 3279.

[9] M.-H. Fang, K.-C. Chen, N. Majewska, T. Leśniewski, S. Mahlik, G. Leniec, S. M. Kaczmarek, C.-W. Yang, K.-M. Lu, H.-S. Sheu, R.-S. Liu, *ACS Energy Lett.* **2020**, *6*, 109.

[10] L. You, R. Tian, T. Zhou, R.-J. Xie, *Chem. Eng. J.* **2021**, *417*, 129224.

[11] Q. Lin, Q. Wang, M. Liao, M. Xiong, X. Feng, X. Zhang, H. Dong, D. Zhu, F. Wu, Z. Mu, *ACS Appl. Mater. Interfaces* **2021**, *13*, 18274.

[12] C. Yuan, R. Li, Y. Liu, L. Zhang, J. Zhang, G. Leniec, P. Sun, Z. Liu, Z. Luo, R. Dong, J. Jiang, *Laser Photonics Rev.* **2021**, DOI: 10.1002/lpor.2021002272100227.

[13] S. Liu, H. Cai, S. Zhang, Z. Song, Z. Xia, Q. Liu, *Mater. Chem. Front.* **2021**, *5*, 3841.

[14] F. He, E. Song, Y. Zhou, H. Ming, Z. Chen, J. Wu, P. Shao, X. Yang, Z. Xia, Q. Zhang, *Adv. Funct. Mater.* **2021**, *31*, 2103743.

[15] C. Freysoldt, B. Grabowski, T. Hickel, J. Neugebauer, G. Kresse, A. Janotti, C. G. Van de Walle, *Rev. Mod. Phys.* **2014**, *86*, 253.